

# ANALYSIS OF A FINITE STATE MULTI-ROTOR DYNAMIC INFLOW MODEL

**J. V. R. Prasad**      **Yong-Boon Kong**

jvr.prasad@ae.gatech.edu      kyongboo@gatech.edu

School of Aerospace Engineering  
Georgia Institute of Technology  
Atlanta, Georgia, USA

**David Peters**

dap@wustl.edu

Mechanical Eng. & Materials Sci.  
Washington University  
Saint Louis, Missouri, USA

## Abstract

Finite state dynamic inflow models are able to compute rotor inflows with reasonable accuracy and has low computational requirements compared to high-fidelity Computational Fluids Dynamics (CFD). As such, they are often used to model rotor inflows in vertical lift vehicle flight simulation for performance and handling qualities evaluations. An extension of the Pressure Potential Superposition Inflow Model (PPSIM) to arbitrary number and arrangement of rotors in a multi-rotor aircraft is explored in this paper. Elements in the apparent mass matrix (M-matrix) and inflow influence coefficient matrix (L-matrix) are functions of separation distances between the rotors in any given configuration. Analysis of differences in steady-state rotor inflow distributions between PPSIM and isolated rotors is carried out. It has been shown that in hover, rotors with small longitudinal (lateral) clearance from one another affect the rotors' inflow distributions, giving rise to fore-to-aft (side-to-side) gradient inflow components. In forward flight, the rotors' wake are swept downstream and mainly affect inflows of rotors operating within the wake.

## 1. NOMENCLATURE

		$\bar{x}, \bar{y}, \bar{z}$	rotor disk coordinates normalised by $R$
$\bar{h}, \bar{d}, \bar{l}$	vertical, longitudinal and lateral separation distances between rotors normalised by $R$ , respectively	$\alpha_j^{rc}, \alpha_j^{rs}$	cosine and sine parts of inflow states, respectively
$[L]$	influence coefficient matrix	$\Delta\lambda_0$	change in uniform inflow component
$[M]$	apparent mass matrix	$\Delta\lambda_{1c}$	change in first harmonic fore-to-aft inflow component
$M, N$	total number of harmonics and radial terms, respectively	$\Delta\lambda_{1s}$	change in first harmonic side-to-side inflow component
$[V_m]$	mass flow parameter	$\mu$	advance ratio
$V_\infty$	free-stream velocity normalised by $\Omega R$	$\nu, \eta, \bar{\psi}$	ellipsoidal coordinates
$R$	rotor radius, ft	$\Omega$	rotor rotational speed, rad/s
$m, r$	harmonic number	$\Psi_j^r$	radial shaping function
$n, j$	polynomial number	$\Phi$	pressure potential
$\bar{P}_n^m, \bar{Q}_n^m$	normalized Legendre functions of the first and second kind, respectively	$\tau_n^{mc}, \tau_n^{ms}$	cosine and sine parts of pressure coefficients, respectively
$\bar{r}$	radial position normalised by $R$	$\xi$	streamline coordinates
$t$	time, seconds	$\vec{\nabla}$	gradient operator
$\bar{t}$	non-dimensional time, $\Omega t$	$(^*)$	derivatives with respect to non-dimensional time, $\bar{t}$
$\vec{v}$	velocity vector	PPSIM	Pressure Potential Superposition Inflow Model
$\bar{w}$	rotor downwash normalised by $\Omega R$		

## 2. INTRODUCTION

In rotorcraft flight simulations, finite state inflow models are used extensively to predict rotor inflows for performance and handling qualities evaluations. One reason is that finite state inflow models are formulated in state-space form, making them convenient to use for aeromechanics analysis as well as control law development. In terms of computational effort, finite state inflow models require less time to compute rotor inflows compared to Computational Fluids Dynamics (CFD) or other wake-capturing software.

For single rotor configuration, the Peters-He<sup>1</sup> inflow model has been shown to correlate well with experimental data<sup>2</sup> and are used in rotorcraft flight simulation software such as FLIGHTLAB<sup>®3</sup> and Rotorcraft Comprehensive Analysis System (RCAS)<sup>4</sup>. In coaxial rotors system, the Pressure Potential Superposition Inflow Model (PPSIM)<sup>5,6,7</sup> is used to predict inflows on upper and lower rotors. Wake distortion and time delay corrections are applied to PPSIM to account for rotor-to-rotor interactions not captured by potential flow<sup>8,9,10</sup>.

As designs of advanced vertical lift vehicles move beyond single and coaxial rotors configurations, there is a need to develop new inflow models to correctly assess effects of rotor inflow dynamics on flight stability of these multi-rotor aircraft. Clearly, extraction of finite state inflow models from flight data is not feasible during the early design phase. Although CFD software can be used to generate the needed rotor inflow distributions for system identification, the computational load required is expensive when iterating between different multi-rotor configurations. What is required is a finite state inflow model that captures interference effects between multiple rotors and still able to compute rotor inflow distributions in a short amount of time. One solution is to develop an analytical finite state multi-rotor dynamic inflow model by extending PPSIM to any number and rotor arrangement.

The main objective of this paper is to study rotor inflows of some realistic multi-rotor configurations using the pressure potential superposition approach. First, formulation of the multi-rotor PPSIM is presented. Next, change in steady-state inflow distribution on each rotor due to perturbations in pressure loading are compared against isolated rotor results, in both hover and forward flight conditions.

## 3. MODELLING

Flow fields around the rotor disks are assumed to be inviscid, irrotational and incompressible. In addition,

rotor wake geometry is rigid and cylindrical in shape. In forward flight, the wake takes on the shape of a skewed cylindrical with average wake skew angle computed using momentum theory.

### 3.1. Multi-rotor Pressure Potential Superposition Inflow Model

Pressure potential inflow model is formulated from continuity and momentum equations of an incompressible potential flow representation given as

$$(1) \quad \vec{\nabla} \cdot \vec{v} = 0$$

$$(2) \quad \frac{\partial \vec{v}}{\partial t} - V_\infty \frac{\partial \vec{v}}{\partial \xi} = -\vec{\nabla} \Phi$$

The on-disk inflow is modelled by using shaping functions,  $\Psi_j^r$  with associated cosine and sine harmonics and unknown inflow coefficients

$$(3) \quad \bar{w} = \sum_r^M \sum_{j=r+1, r+3, \dots}^N \Psi_j^r(\nu) [\alpha_j^{rc} \cos(r\bar{\psi}) + \alpha_j^{rs} \sin(r\bar{\psi})]$$

$$(4) \quad \Psi_j^r(\nu) = \frac{\bar{P}_j^r(\nu)}{\nu}$$

In addition, the pressure term  $\Phi$ , in equation (2) is expanded in terms of Legendre polynomials and harmonic functions

$$(5) \quad \Phi = \sum_m^M \sum_{n=m+1, m+3, \dots}^N \bar{P}_n^m(\nu) \bar{Q}_n^m(\eta) [\tau_n^{mc} \cos(m\bar{\psi}) + \tau_n^{ms} \sin(m\bar{\psi})]$$

By considering the pressure field to be sum of individual pressure of all rotors, and using the shaping function expansion of induced velocities corresponding to each rotor, the relationship between inflow states and pressure coefficients is obtained after substituting equations (3) through (5) into equation (2). The resulting set of equations for multi-rotor Pressure Potential Superposition Inflow Model (PPSIM) can be written in general form as

$$(6) \quad \begin{bmatrix} M_{11} & \cdots & M_{1N} \\ \vdots & \ddots & \vdots \\ M_{N1} & \cdots & M_{NN} \end{bmatrix} \begin{Bmatrix} \alpha_1^* \\ \vdots \\ \alpha_N^* \end{Bmatrix} + [V_m] \begin{bmatrix} L_{11} & \cdots & L_{1N} \\ \vdots & \ddots & \vdots \\ L_{N1} & \cdots & L_{NN} \end{bmatrix}^{-1} \begin{Bmatrix} \alpha_1 \\ \vdots \\ \alpha_N \end{Bmatrix} = \begin{Bmatrix} \frac{\tau_1}{2} \\ \vdots \\ \frac{\tau_N}{2} \end{Bmatrix}$$

In equation (6),  $\alpha_1$  and  $\alpha_N$  are column vectors of inflow states corresponding to rotor 1 and rotor N, respectively, while  $\tau_1$  and  $\tau_N$  are pressure coefficient column vectors of rotor 1 and rotor N, respectively. In addition,  $[V_m]$  is a diagonal matrix consisting of each rotor's mass flow parameter, i.e.  $\text{diag}([V_{m1}], \dots, [V_{mN}])$ .

The M- and L-matrices are known as the apparent mass and influence coefficient matrices, respectively. Diagonal blocks in M- and L-matrices relate self-induced inflow states due to the rotor's own pressure coefficients. Rotor-to-rotor coupling due to mutual interactions between different rotors are captured by the off-diagonal blocks, which are functions of separation distances between the rotors. The first subscript in M- and L-matrices blocks corresponds to the rotor where inflow states are to be computed or also known as the 'Receiving' rotor. Second subscript in the blocks refers to the rotor where effect of pressure coefficients are to be considered or known as the 'Active' rotor. For example,  $L_{12}$  relates influence of rotor 2 pressure loading on rotor 1 inflow states.

Since calculation of the M- and L-matrices elements involves two rotors, it is appropriate to define the coordinate system used in PPSIM for consistency. As shown in Fig. 1, the reference coordinate system is located at the 'Receiving' rotor's hub. The 'Active' rotor is located at some distances away from the 'Receiving' rotor along the vertical or Z-axis ( $\bar{h}$ ), longitudinal or X-axis ( $\bar{d}$ ) and lateral or Y-axis ( $\bar{l}$ ) directions, respectively. These distances are normalised with respect to the 'Receiving' rotor radius.

Finally, elements in the M- and L-matrices off-diagonal blocks are computed by numerical integrations of equations (7) through (12). In these equations, coordinate system corresponding to the 'Receiving' rotor is denoted as 'R' whereas those corresponding to the 'Active' rotor is denoted as 'A'. As an example, elements in  $L_{12}$  are computed by treating rotor 1 as the 'Receiving' rotor and rotor 2 as the 'Active' rotor. On a similar token, elements in  $L_{21}$  are computed by treating rotor 2 as the 'Receiving' rotor and rotor 1 as the 'Active' rotor. Note that the order of rotor indexing in a multi-rotor configuration is arbitrary.

By definition, M-matrix is inverse of the E-operator such that  $[M] = [E]^{-1}$ . Each element in  $[E_{RA}]$

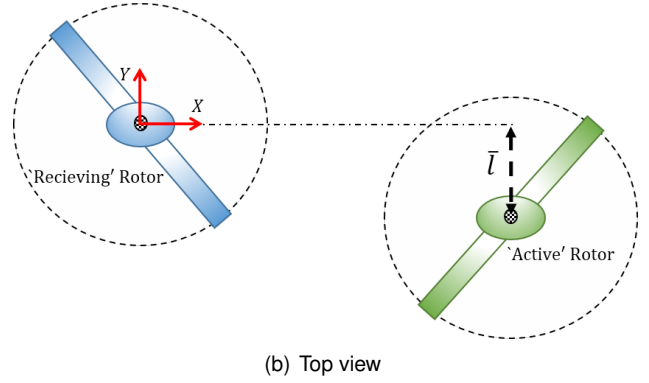
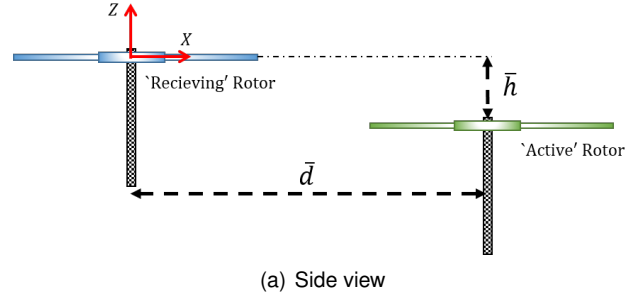


Figure 1: Coordinate system used to compute elements in PPSIM M- and L-matrices

is

$$(7) \quad E_{jn,\cos}^{0m} = \frac{1}{2\pi} \int_0^{2\pi} \int_0^1 \nu_R \bar{P}_j^0(\nu_R) * \frac{\partial(\bar{P}_n^m(\nu_A) \bar{Q}_n^m(\eta_A) \cos(m\bar{\psi}_A))}{\partial \bar{z}_R} d\nu_R d\bar{\psi}_R$$

$$(8) \quad E_{jn,\cos}^{rm} = \frac{1}{\pi} \int_0^{2\pi} \int_0^1 \nu_R \bar{P}_j^r(\nu_R) \cos(r\bar{\psi}_R) * \frac{\partial(\bar{P}_n^m(\nu_A) \bar{Q}_n^m(\eta_A) \cos(m\bar{\psi}_A))}{\partial \bar{z}_R} d\nu_R d\bar{\psi}_R$$

$$(9) \quad E_{jn,\sin}^{rm} = \frac{1}{\pi} \int_0^{2\pi} \int_0^1 \nu_R \bar{P}_j^r(\nu_R) \sin(r\bar{\psi}_R) * \frac{\partial(\bar{P}_n^m(\nu_A) \bar{Q}_n^m(\eta_A) \sin(m\bar{\psi}_A))}{\partial \bar{z}_R} d\nu_R d\bar{\psi}_R$$

For elements in  $[L_{RA}]$

$$(10) \quad L_{jn,\cos}^{0m} = \frac{1}{2\pi} \int_0^{2\pi} \int_0^1 \nu_R \bar{P}_j^0(\nu_R) * \int_0^\infty \frac{\partial(\bar{P}_n^m(\nu_A) \bar{Q}_n^m(\eta_A) \cos(m\bar{\psi}_A))}{\partial \bar{z}_R} d\xi_A d\nu_R d\bar{\psi}_R$$

$$(11) \quad L_{jn,\cos}^m = \frac{1}{\pi} \int_0^{2\pi} \int_0^1 \nu_R \bar{P}_j^r(\nu_R) \cos(r\bar{\psi}_R) * \int_0^\infty \frac{\partial(\bar{P}_n^m(\nu_A) \bar{Q}_n^m(\eta_A) \cos(m\bar{\psi}_A))}{\partial \bar{z}_R} d\xi_A d\nu_R d\bar{\psi}_R$$

$$(12) \quad L_{jn,\sin}^m = \frac{1}{\pi} \int_0^{2\pi} \int_0^1 \nu_R \bar{P}_j^r(\nu_R) \sin(r\bar{\psi}_R) * \int_0^\infty \frac{\partial(\bar{P}_n^m(\nu_A) \bar{Q}_n^m(\eta_A) \sin(m\bar{\psi}_A))}{\partial \bar{z}_R} d\xi_A d\nu_R d\bar{\psi}_R$$

Wake contraction effects are taken into account by correcting the streamline coordinates when computing elements in the L-matrix. These pre-computed elements are then stored in a lookup table indexed by average wake skew angle for use in real-time flight simulations.

#### 4. SIMULATION SETUP

PPSIM is implemented and executed in MATLAB® simulation environment. Since the formulation of finite state inflow models is based on perturbation theory, it makes sense to investigate changes in inflow distributions due to small perturbations on the rotors' loadings about some steady flight condition. Furthermore, it has been shown in Ref. 9 that PPSIM perturbed inflow results are insensitive to initial flight conditions, making the analysis straightforward. In this study, pressure coefficients and mass flow parameters characteristic of the steady flight conditions were used. Changes in steady-state inflow distributions from PPSIM are compared against isolated rotor results (computed using the Peters-He inflow model) to investigate effects of rotor-to-rotor coupling due to pressure coefficients perturbations. In addition, 15 inflow states were used in PPSIM and Peters-He inflow model.

##### 4.1. Description of rotor configurations

In order to analyse effects of rotor-to-rotor coupling in advanced multi-rotor configurations, a few realistic rotor arrangements were used in this study. A total of three configurations were chosen for evaluation; two configurations have 2 rotors each and the third configuration has a total of 3 rotors. All rotors have the same radius and free-stream is from left to right as shown in Figs. 2 through 4.

For the 2 rotors arrangement, both rotors are vertically separated by a distance of  $0.19R$  with no lateral separation. They are separated longitudinally by a distance of  $1.5R$  and  $2.5R$  as shown in Figs. 2 and 3, respectively. The upper rotor is denoted as

'Rotor 1' while the lower rotor is denoted as 'Rotor 2'. Arrangement of the 3 rotors configuration is shown in Fig. 4 where the lateral rotors are equally spaced apart from the center rotor by a distance of  $1.5R$ . The center rotor is denoted as 'Rotor 1', while the lateral rotor closer to the bottom of the picture is labeled 'Rotor 2' and the other one labeled as 'Rotor 3'.

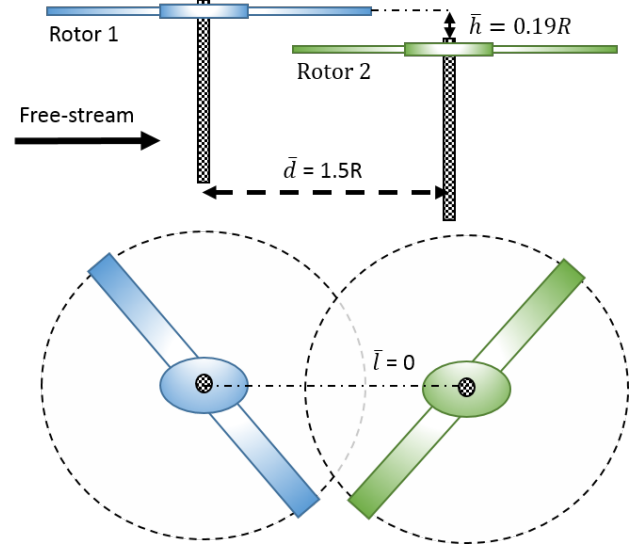


Figure 2: Configuration 1

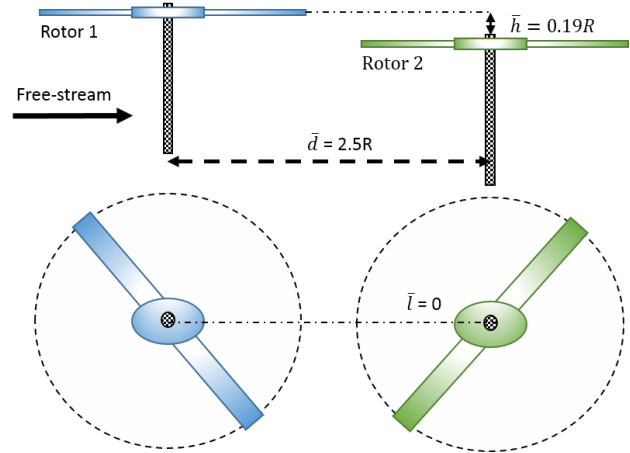


Figure 3: Configuration 2

#### 5. RESULTS AND ANALYSIS

On-disk inflow predictions from PPSIM are compared against isolated rotor results for Configurations 1 to 3 at different steady flight conditions. While contour plots of inflow distributions provide insights on qualitative differences between the models, inflow variations give a more meaningful quantitative comparison. Inflow variations are extracted from changes in rotor inflow distributions,  $\Delta \bar{w}(\bar{r}, \bar{\psi})$  using equations (13) through (15) where  $\Delta \lambda_0$ ,  $\Delta \lambda_{1c}$  and

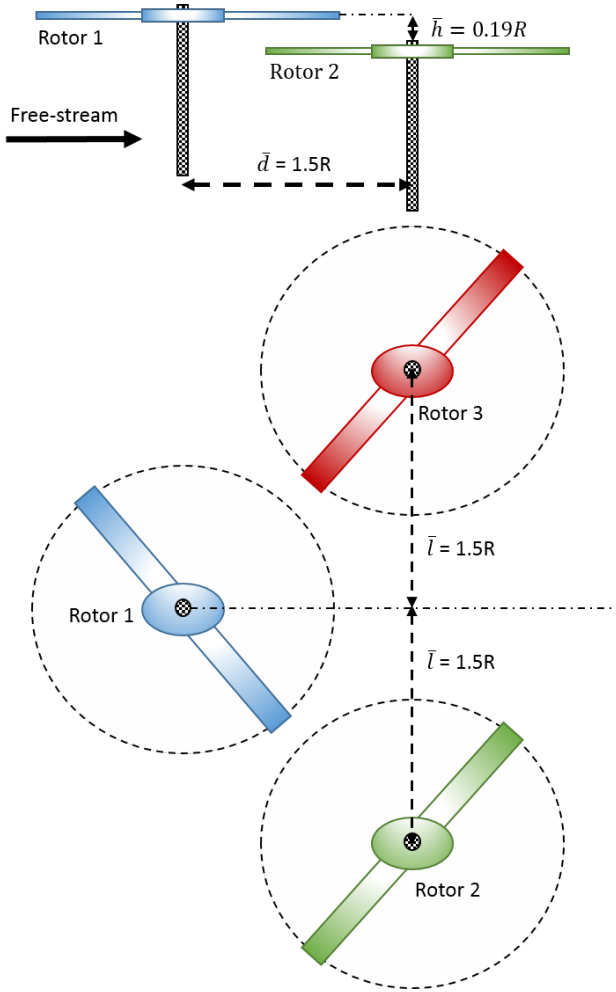


Figure 4: Configuration 3

$\Delta\lambda_{1s}$  are changes in uniform inflow, fore-to-aft gradient and side-to-side gradient inflow components, respectively.

$$(13) \quad \Delta\lambda_0 = \frac{1}{\pi} \int_0^{2\pi} \int_0^1 \Delta\bar{w}(\bar{r}, \bar{\psi}) \bar{r} d\bar{r} d\bar{\psi}$$

$$(14) \quad \Delta\lambda_{1c} = \frac{4}{\pi} \int_0^{2\pi} \int_0^1 \Delta\bar{w}(\bar{r}, \bar{\psi}) \bar{r}^2 \cos(\psi) d\bar{r} d\bar{\psi}$$

$$(15) \quad \Delta\lambda_{1s} = \frac{4}{\pi} \int_0^{2\pi} \int_0^1 \Delta\bar{w}(\bar{r}, \bar{\psi}) \bar{r}^2 \sin(\psi) d\bar{r} d\bar{\psi}$$

In the following results, all rotors are subjected to the same amount of perturbations on their pressure loadings. For this study, only uniform pressure coefficient,  $\tau_1^{0c}$  is perturbed because it is directly related to the rotor's thrust coefficient. Thrust generation capability is one of the key design factor of any vertical lift vehicle, especially in a multi-rotor

configuration where rotor-to-rotor coupling has a significant impact on its performance<sup>11</sup>.

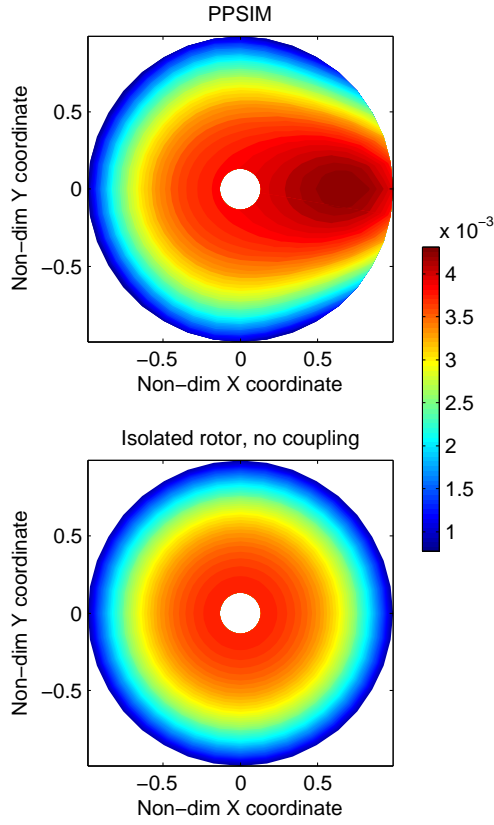
### 5.1. Comparison of inflow distributions for Configuration 1

A comparison of the changes in Rotor 1 and Rotor 2 steady-state inflow distributions in hover between PPSIM and the isolated rotors (no rotor-to-rotor coupling) due to  $\tau_1^{0c}$  perturbations on both rotors are shown in Figs. 5 and 6, respectively. In Fig. 5(a), the top subplot shows Rotor 1's inflow distribution computed using PPSIM compared against an isolated rotor shown in the bottom subplot. The main difference observed in PPSIM result is that inflow distribution is no longer axisymmetric due to the coupling effect from Rotor 2, even though it is operating in hover flight condition. In fact, the inflow distribution is somewhat similar to that of forward flight due to a longitudinal separation between the upper and lower rotors. Inflow variations on Rotor 1 between PPSIM and that of an isolated rotor is presented in the form of a bar chart in Fig. 5(b). As expected, the fore-to-aft gradient inflow component corresponding to PPSIM is non-zero with slight increase in uniform inflow component due to interference effects from Rotor 2. Next, Fig. 6 shows the comparison of inflow distribution on Rotor 2 under hover flight condition. Similarly, the contour plot in Fig. 6(a) shows that Rotor 2's asymmetric inflow distribution is distorted by inflows from Rotor 1 in PPSIM results. This shows up as a non-zero fore-to-aft gradient inflow component in PPSIM for Rotor 2 as seen in Fig. 6(b).

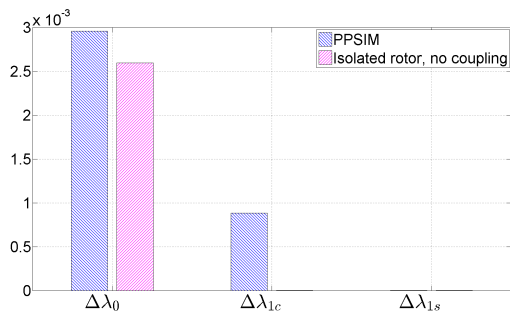
Next, on-disk inflow distribution comparisons between PPSIM and isolated rotors are investigated at an advance ratio of 0.12. Unlike in hover flight, no significant coupling effects on Rotor 1 due to Rotor 2 are observed in Fig. 7. This is mainly because wake from Rotor 2 is swept downstream, which has little impact on induced velocities on Rotor 1. On the other hand, Rotor 2 operates within Rotor 1's wake and hence experiences significant inflow coupling effects from Rotor 1. In Fig. 8(a), footprint from Rotor 1's skewed wake can be clearly seen on Rotor 2's inflow distribution when compared against the isolated rotor. This resulted in an increase of Rotor 2's uniform inflow component as shown in Fig. 8(b).

### 5.2. Comparison of inflow distributions for Configuration 2

For Configuration 2 operating in hover condition, rotor-to-rotor coupling effects between Rotor 1 and Rotor 2 are nearly negligible as shown in Figs. 9 and 10. Axisymmetric inflow distributions for both Rotor 1 and Rotor 2 are clearly observed in PPSIM

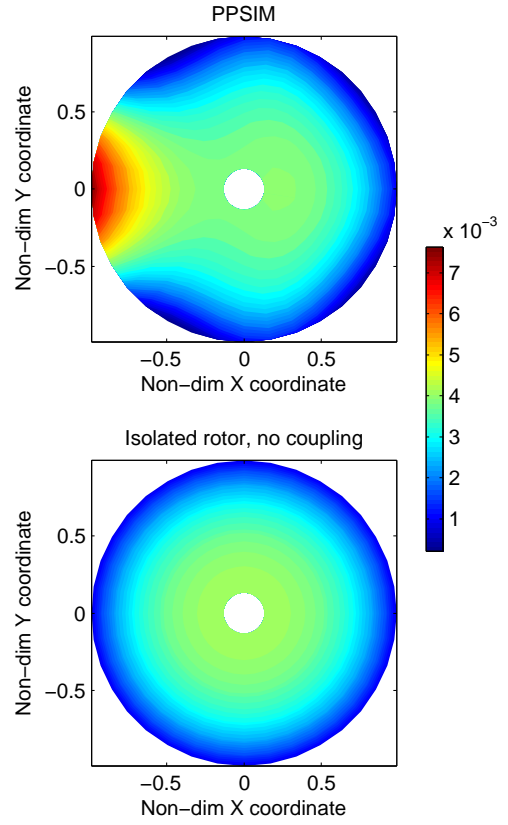


(a) Contour plots of inflow distribution

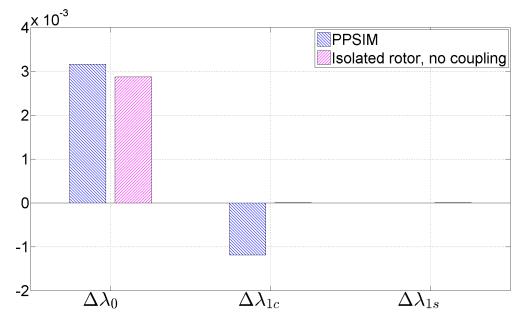


(b) Bar chart of inflow variations

Figure 5: Change in steady-state inflow distribution on Rotor 1 of Configuration 1 in hover, due to  $\tau_1^{0c}$  perturbation

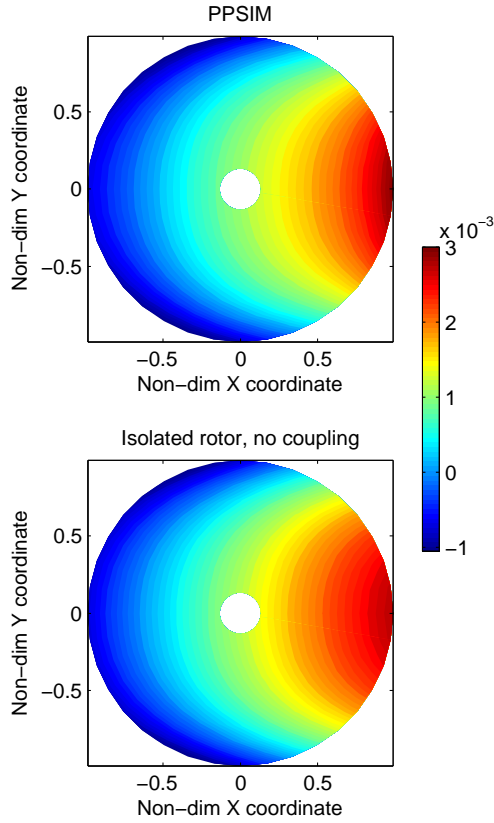


(a) Contour plots of inflow distribution

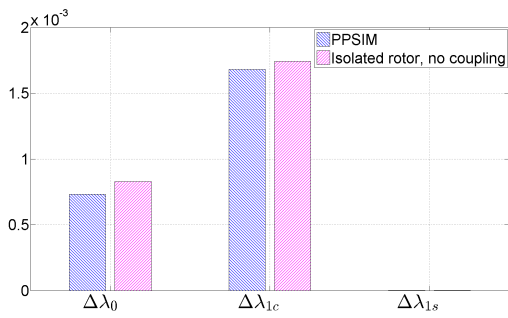


(b) Bar chart of inflow variations

Figure 6: Change in steady-state inflow distribution on Rotor 2 of Configuration 1 in hover, due to  $\tau_1^{0c}$  perturbation

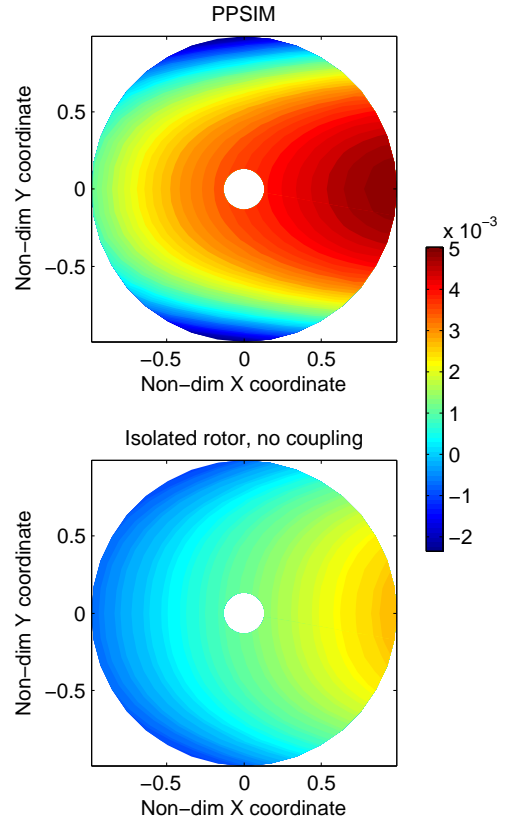


(a) Contour plots of inflow distribution

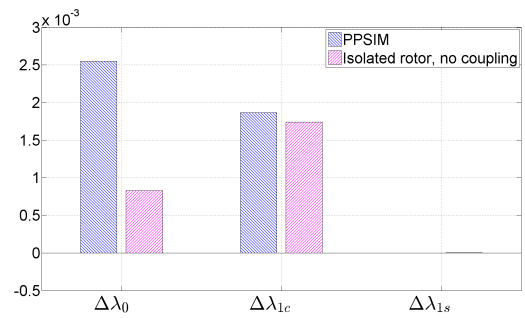


(b) Bar chart of inflow variations

Figure 7: Change in steady-state inflow distribution on Rotor 1 of Configuration 1 at  $\mu = 0.12$ , due to  $\tau_1^{0c}$  perturbation



(a) Contour plots of inflow distribution



(b) Bar chart of inflow variations

Figure 8: Change in steady-state inflow distribution on Rotor 2 of Configuration 1 at  $\mu = 0.12$ , due to  $\tau_1^{0c}$  perturbation

results with very small fore-to-aft gradient inflow variations; unlike the results seen in Configuration 1. The main reason is that there is no overlap between Rotor 1 and Rotor 2 disk areas in Configuration 2 (see Fig. 3). As such, wake effects from Rotor 1 have little impact on Rotor 2's induced velocities. On a similar token, Rotor 2's wake is far away from Rotor 1 to have any significant effect on it during hover flight condition.

At advance ratio of 0.12, rotor-to-rotor coupling effects are again observed on Rotor 2 in PPSIM results in Fig. 12. This is because of the skewed wake from Rotor 1 impacting on Rotor 2, which did not occur during hover or at low advance ratios. From Fig. 12(b), skewed wake effects from Rotor 1 increase Rotor 2's uniform inflow component, which is to be expected. A slight drop in Rotor 2's fore-to-aft gradient inflow component is also observed, which is likely due to partial overlap between Rotor 1's skewed wake and Rotor 2 disk area, i.e. the skewed wake mainly overlaps the disk's fore region. As seen from Fig. 11, Rotor 1 is not significantly affected by Rotor 2 as its wake is swept downstream.

### **5.3. Comparison of inflow distributions for Configuration 3**

In Configuration 3, the rotors have very little coupling effects when operating in hover because there are no overlap of disk areas between them. As such, their inflow distributions are similar to that of an isolated rotor. In forward flight, coupling effects from Rotor 2 and Rotor 3 have small influences on Rotor 1 inflow distribution as shown in Fig. 13. On the other hand, Rotor 1's wake overlaps the other rotors' disk near the edge. This changes Rotor 2's and Rotor 3's inflow distributions significantly as shown in Figs. 14(a) and 15(a), respectively. Although there is an increase of inflow at the region where the wake overlaps the disk area, there is also a shift of high (low) inflow region at the disk aft (fore). Interestingly, due to this offset, there are very small changes to Rotor 2's and Rotor 3's side-to-side gradient inflow components seen in Figs. 14(b) and Figs. 15(b), respectively.

## **6. CONCLUDING REMARKS**

A finite state inflow model for multi-rotor configurations has been developed analytically using the pressure potential superposition approach. The M- and L-matrices in the Pressure Potential Superposition Inflow Model (PPSIM) are functions of number and separation distances between the rotors. As such, PPSIM is applicable to any generic vertical lift configurations for rotor inflow distribution predictions. Furthermore, PPSIM is formulated in

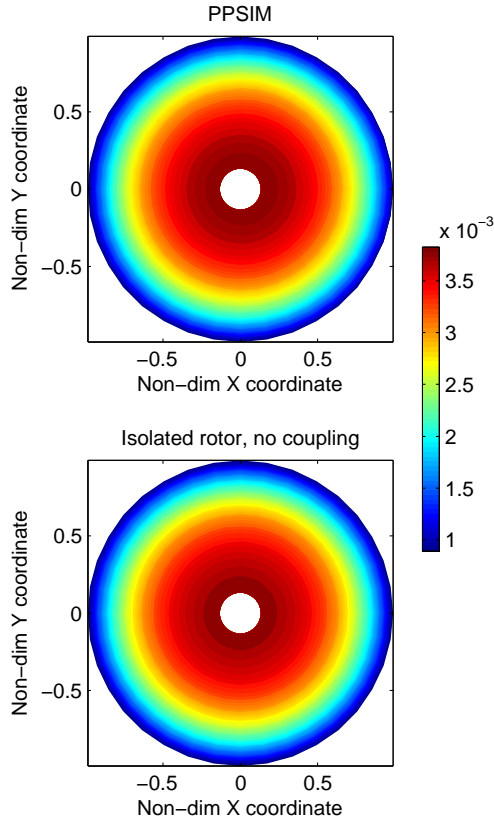
state-space form which can be used in eigenvalues analysis for flight stability evaluations.

In this study, steady-state inflow distributions from three types of advanced rotorcraft configurations are considered. For rotors with overlap disk areas between upper and lower rotors, rotor-to-rotor coupling effects distorted the otherwise axisymmetric inflow distributions on both rotors in hover. This resulted in both rotors having non-zero fore-to-aft (side-to-side) gradient inflow components in hover. On the other hand, if the rotors are sufficiently separated, each rotor can be treated as an isolated rotor with negligible coupling effects. In forward flight, wake effects due to downstream rotors have little influences on upstream rotors' inflow distributions because the wakes are propagated away by the free-stream. For rotors that operate within wakes generated by other rotors, effects on their inflow variations will depend on the amount of overlap region between the wake and the rotor disk.

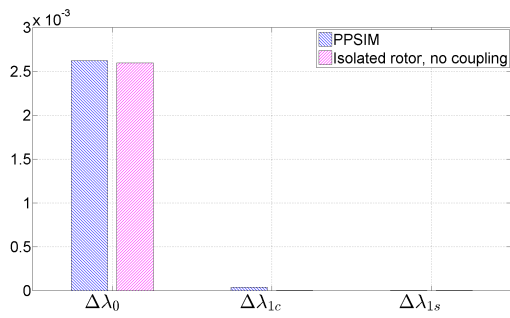
Analysis of steady-state inflow distribution differences between PPSIM and isolated rotors has been carried out on various multi-rotor designs. The next step is to compare steady-state results from PPSIM against high-fidelity Computational Fluids Dynamics (CFD) or free-wake capturing software inflow predictions. This allows calculation of corrections to PPSIM L-matrix to account for any rotor-to-rotor wake distortion effects.

## **7. ACKNOWLEDGMENTS**

This study is supported under the NRTC Vertical Lift Rotorcraft Center of Excellence (VLRCOE) from the U.S. Army Aviation and Missile Research, Development and Engineering Center (AMRDEC) under Technology Investment Agreement W911W6-17-2-0002, entitled Georgia Tech Vertical Lift Research Center of Excellence (GT-VLRCOE) with Dr. Mahendra Bhagwat as the Program Manager. The authors would like to acknowledge that this research and development was accomplished with the support and guidance of the NRTC. The views and conclusions contained in this document are those of the authors and should not be interpreted as representing the official policies, either expressed or implied, of the AMRDEC or the U.S. Government. The U.S. Government is authorized to reproduce and distribute reprints for Government purposes notwithstanding any copyright notation thereon.

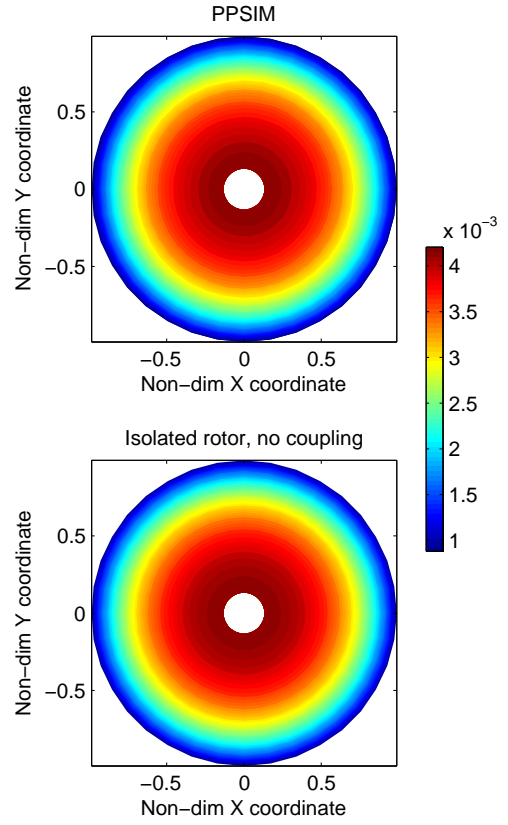


(a) Contour plots of inflow distribution

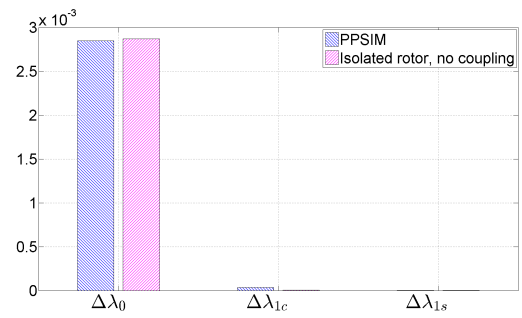


(b) Bar chart of inflow variations

Figure 9: Change in steady-state inflow distribution on Rotor 1 of Configuration 2 in hover, due to  $\tau_1^{0c}$  perturbation

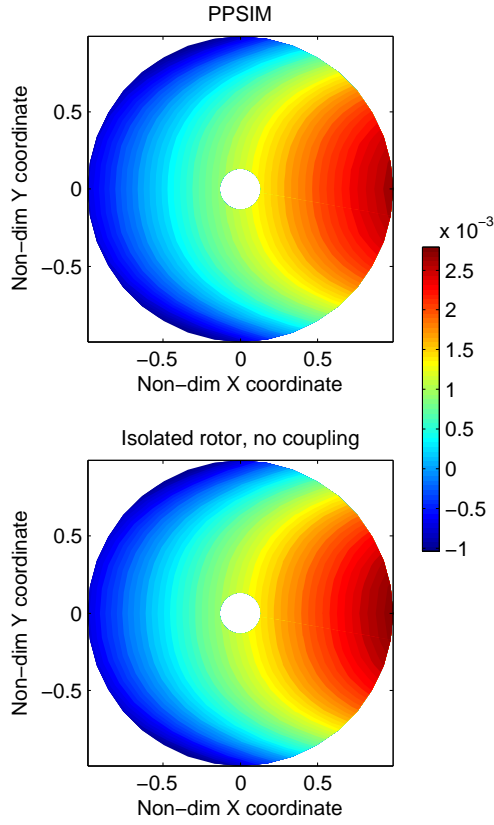


(a) Contour plots of inflow distribution

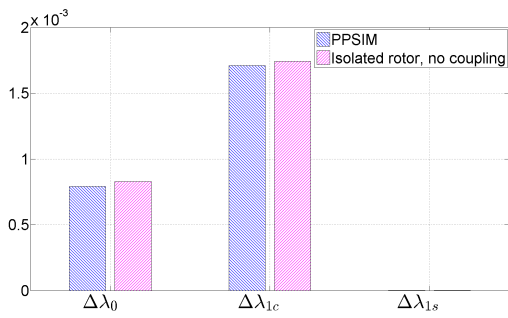


(b) Bar chart of inflow variations

Figure 10: Change in steady-state inflow distribution on Rotor 2 of Configuration 2 in hover, due to  $\tau_1^{0c}$  perturbation

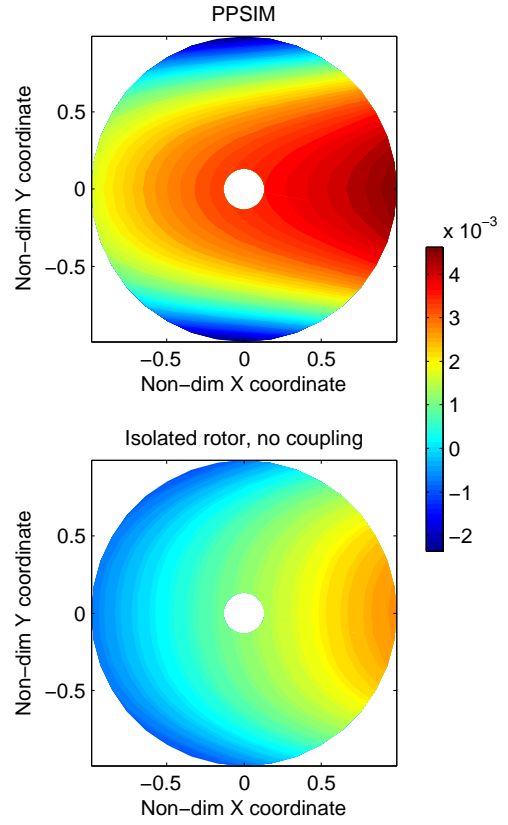


(a) Contour plots of inflow distribution

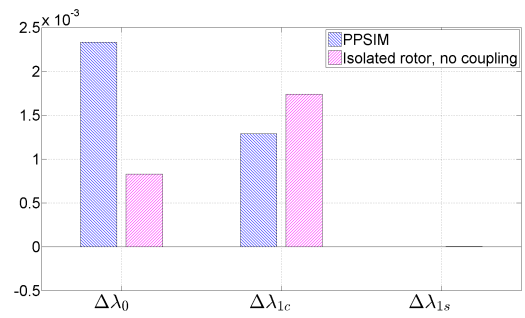


(b) Bar chart of inflow variations

Figure 11: Change in steady-state inflow distribution on Rotor 1 of Configuration 2 at  $\mu = 0.12$ , due to  $\tau_1^{0c}$  perturbation

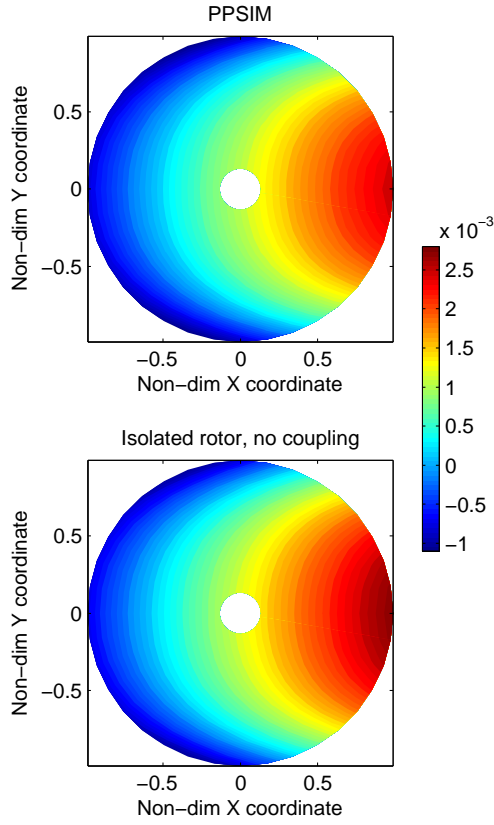


(a) Contour plots of inflow distribution

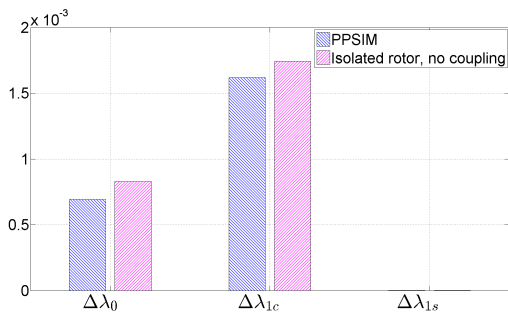


(b) Bar chart of inflow variations

Figure 12: Change in steady-state inflow distribution on Rotor 2 of Configuration 2 at  $\mu = 0.12$ , due to  $\tau_1^{0c}$  perturbation

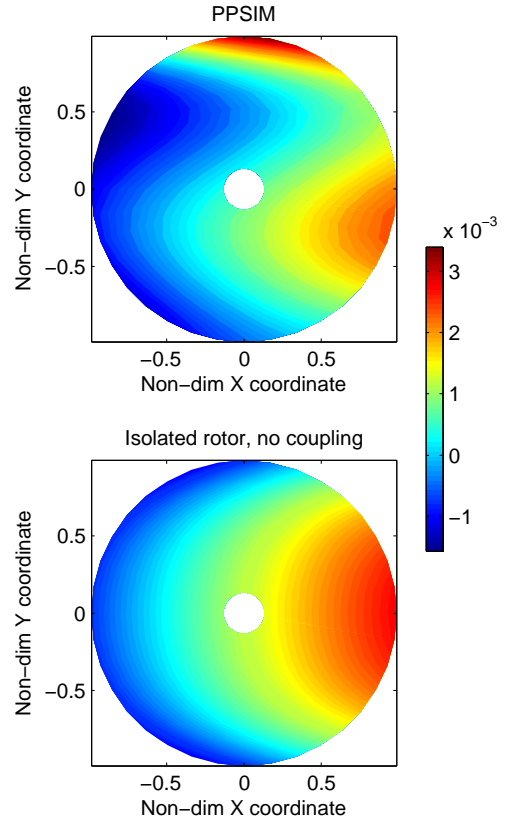


(a) Contour plots of inflow distribution

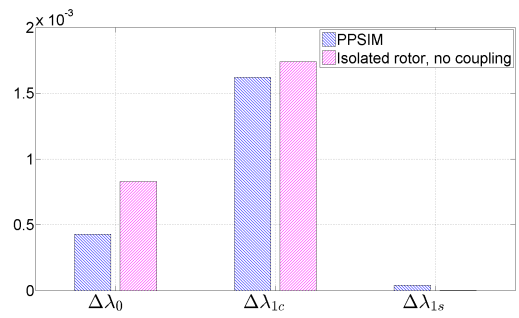


(b) Bar chart of inflow variations

Figure 13: Change in steady-state inflow distribution on Rotor 1 of Configuration 3 at  $\mu = 0.12$ , due to  $\tau_1^{0c}$  perturbation



(a) Contour plots of inflow distribution

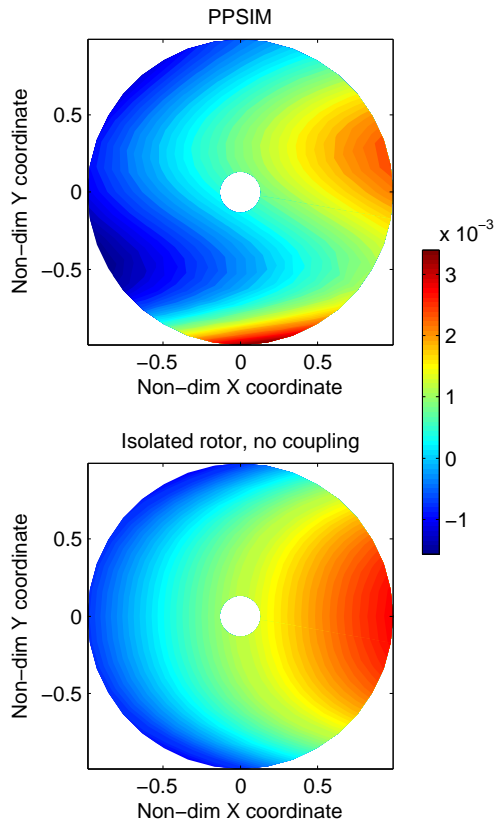


(b) Bar chart of inflow variations

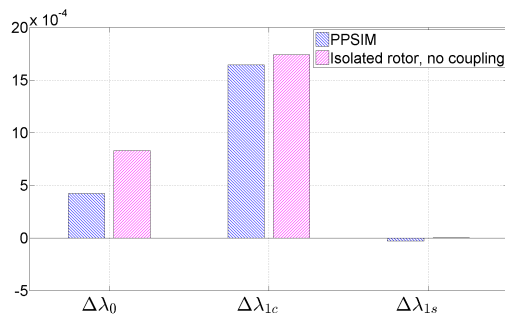
Figure 14: Change in steady-state inflow distribution on Rotor 2 of Configuration 3 at  $\mu = 0.12$ , due to  $\tau_1^{0c}$  perturbation

## 8. REFERENCES

- [1] He, C. and Peters, D., "An aeroelastic analysis with a generalised wake," in *Proceedings of the AHS International Technical Specialist's Meeting on Rotorcraft Basic Research*, Mar. 1981.
- [2] Peters, D. and He, C., "Correlation of measured induced velocities with a finite-state wake model," in *Presented at the AHS Aeromechanics Specialist's Conference, San Francisco, California*, Jan. 2010.
- [3] Advanced Rotorcraft Technology, Inc., *FLIGHTLAB X-Analysis user manual*, July 2013.
- [4] US Army Research, Development, and Engineering Command, *Rotorcraft Comprehensive Analysis System user's manual*, Aug. 2012.
- [5] Nowak, M., Prasad, J. V. R., Xin, H., and Peters, D. A., "A potential flow model for coaxial rotors in forward flight," in *Proceedings of the 39th European Rotorcraft Forum, Moscow, Russia*, Sept. 2013.
- [6] Nowak, M., Prasad, J. V. R., and Peters, D., "Development of a finite state model for a coaxial rotor in forward flight," in *Proceedings of the AHS 70th Annual Forum*, May 2014.
- [7] Prasad, J. V. R., Kong, Y. B., and Peters, D. A., "Analytical methods for modeling inflow dynamics of a coaxial rotor system," in *Proceedings of the 42nd European Rotorcraft Forum, Lille, France*, Sept. 2016.
- [8] Kong, Y. B., Prasad, J. V. R., and He, C., "Analysis of a finite state coaxial rotor inflow model," in *Proceedings of the 41st European Rotorcraft Forum*, Sept. 2015.
- [9] Kong, Y. B., Prasad, J. V. R., Sankar, L. N., and Peters, D. A., "Finite state coaxial rotor inflow model system identification using perturbation approach," in *Presented at the Asia-Australian Rotorcraft Forum, Singapore*, Nov. 2016.
- [10] Kong, Y. B., Prasad, J. V. R., and Peters, D. A., "Development of a finite state dynamic inflow model for coaxial rotors using analytical methods," in *Presented at the AHS 73rd Annual Forum, Fort Worth, Texas*, May 2017.
- [11] Dingeldein, R., "Wind tunnel studies of the performance of multicopter configurations," NASA TN 3226, Aug. 1954.



(a) Contour plots of inflow distribution



(b) Bar chart of inflow variations

Figure 15: Change in steady-state inflow distribution on Rotor 3 of Configuration 3 at  $\mu = 0.12$ , due to  $\tau_1^{0c}$  perturbation

**Copyright Statement**

The author(s) confirm that they, and/or their company or organization, hold copyright on all of the original material included in this paper. The author(s) also confirm that they have obtained permission, from the copyright holder of any third party material included in this paper, to publish it as part of their paper. The author(s) confirm that they give permission, or have obtained permission from the copyright holder of this paper, for the publication and distribution of this paper as part of the ERF proceedings or as individual offprints from the proceedings and for inclusion in a freely accessible web-based repository.